Accepted in Astrophysical Journal
Preprint typeset using LaTeX style emulateapj v. 5/2/11



# ALIGNMENT BETWEEN FLATTENED PROTOSTELLAR INFALL ENVELOPES AND AMBIENT MAGNETIC FIELDS

Nicholas L. Chapman[1], Jacqueline A. Davidson[2], Paul F. Goldsmith[3], Martin Houde[4,5], Woojin Kwon[6,7], Zhi-Yun Li[8], Leslie W. Looney[6], Brenda Matthews[9,10], Tristan G. Matthews[1], Giles Novak[1], Ruisheng Peng[11], John E. Vaillancourt[12], Nikolaus H. Volgenau[13]

*Accepted in Astrophysical Journal*

## ABSTRACT

We present 350 $\mu$m polarization observations of four low-mass cores containing Class 0 protostars: L483, L1157, L1448-IRS2, and Serp-FIR1. This is the second paper in a larger survey aimed at testing magnetically regulated models for core-collapse. One key prediction of these models is that the mean magnetic field in a core should be aligned with the symmetry axis (minor axis) of the flattened YSO inner envelope (aka pseudodisk). Furthermore, the field should exhibit a pinched or hour-glass shaped morphology as gravity drags the field inward towards the central protostar. We combine our results for the four cores with results for three similar cores that were published in the first paper from our survey. An analysis of the 350 $\mu$m polarization data for the seven cores yields evidence of a positive correlation between mean field direction and pseudodisk symmetry axis. Our rough estimate for the probability of obtaining by pure chance a correlation as strong as the one we found is about 5%. In addition, we combine together data for multiple cores to create a source-averaged magnetic field map having improved signal-to-noise ratio, and this map shows good agreement between mean field direction and pseudodisk axis (they are within 15°). We also see hints of a magnetic pinch in the source-averaged map. We conclude that core-scale magnetic fields appear to be strong enough to guide gas infall, as predicted by the magnetically regulated models. Finally, we find evidence of a positive correlation between core magnetic field direction and bipolar outflow axis.

## 1. INTRODUCTION

Star formation occurs in molecular clouds. Even though these clouds are relatively large, with sizes ∼few parsecs, they are gravitationally bound. Despite being bound, the inferred rate of star formation in the clouds is less than that estimated from gravitational free-fall collapse. To explain this discrepancy, a mechanism is needed to regulate the star formation rate. Two such mechanisms that have been proposed are magnetic support and turbulence. See, e.g., McKee & Ostriker (2007) for a review of these issues. This turbulence is often modeled as being super-Alfvénic, though trans-Alfvénic turbulence may also act to suppress star formation (Federrath & Klessen 2013).

Embedded within molecular clouds are individual cores (typically ∼20,000 AU in size for low-mass cores), each of which could potentially collapse to form a star or group of stars. Besides their possible role in supporting clouds against gravity, magnetic fields may also strongly affect the evolution of these individual cores. Magnetically regulated core-collapse models (Shu et al. 1987; Galli & Shu 1993a,b; Tomisaka 1998; Allen et al. 2003a,b; Shu et al. 2004) treat star formation in low-mass cores where magnetic fields are dynamically important compared to turbulence. These models have two key features which can be observationally tested. First, there should exist a flattened inner core having a size of a few thousand AU, known as a pseudodisk. This pseudodisk is not a rotationally supported disk, but instead is formed by the preferential collapse of material along magnetic field lines as opposed to across field lines. Thus, the core magnetic field should be parallel to the symmetry (minor) axis of the pseudodisk. Secondly, the magnetic field inside the infall radius should have a pinched hourglass morphology. Outside the infall radius, the magnetic field should be uniform or only gently pinched.

A third observational test is to compare the axis of the bipolar outflow with the core magnetic field direction. Outflows are believed to be launched from the inner regions of Keplerian circumstellar disks, with the outflow axes aligned with the rotation axes of the disks (e.g., Konigl & Pudritz 2000; Shu et al. 2000). If such disks form with their rotation axes aligned with the core-scale

[1] Center for Interdisciplinary Exploration and Research in Astrophysics (CIERA) & Dept. of Physics & Astronomy, Northwestern University, 2145 Sheridan Road, Evanston, IL 60208
[2] School of Physics, University of Western Australia, 35 Stirling Hwy, Crawley, WA 6009, Australia
[3] Jet Propulsion Laboratory, California Institute of Technology, 4800 Oak Grove Drive, MS 264-782, Pasadena, CA 91109
[4] Department of Physics and Astronomy, University of Western Ontario, London, ON, Canada
[5] Division of Physics, Mathematics and Astronomy, California Institute of Technology, Pasadena, CA 91125
[6] Department of Astronomy, University of Illinois, 1002 West Green Street, Urbana, IL 61801
[7] SRON Netherlands Institute for Space Research, Landleven 12, 9747 AD, Groningen, The Netherlands
[8] Astronomy Department, University of Virginia, Charlottesville, VA 22904
[9] Herzberg Institute of Astrophysics, National Research Council of Canada, 5071 West Saanich Road, Victoria, BC V9E 2E7, Canada
[10] Department of Physics and Astronomy, University of Victoria, 3800 Finnerty Road, Victoria, BC V8P 1A1, Canada
[11] Caltech Submillimeter Observatory, 111 Nowelo Street, Hilo, HI 96720
[12] SOFIA Science Center, Universities Space Research Association, NASA Ames Research Center, MS 232-11, Moffett Field, CA 94035-0001
[13] California Institute of Technology, Owens Valley Radio Observatory, Big Pine, CA 93513

field, then one might expect a positive correlation between outflow axes and core magnetic fields. However, the theoretical expectation regarding the alignment of circumstellar disk axes with core fields is unsettled at this time. On the one hand, since magnetic braking proceeds faster for angular momentum components perpendicular to a near-uniform, large-scale field during cloud core contraction before collapse (e.g., Mouschovias & Paleologou 1979), one might expect that the rotation axis of the core and circumstellar disk should align with the core magnetic field. This point of view is advocated in § 4.3 of Allen et al. (2003a). However, it is not currently understood how a rotationally supported disk can form at all in this scenario, since magnetic braking in a collapsing core should remove angular momentum sufficiently rapidly to prevent disk formation (e.g., Mellon & Li 2008). Recent simulations of magnetized core collapse by Joos et al. (2012) suggest that circumstellar disks can form more easily if the core magnetic field and core rotation axis are not aligned. In such a scenario, it seems unlikely that disks would form with their axes preferentially parallel to the core magnetic field.

The direction of the plane of the sky component of the magnetic field can be observed through polarization measurements. Interstellar dust grains align with their long axes preferentially perpendicular to the local magnetic field. Polarization arises because the dust grains preferentially absorb and emit radiation with the electric field vector parallel to the grain's long axis. At optical and near-infrared wavelengths, one observes polarized absorption of background starlight seen through a cloud. Thus, the inferred magnetic field is parallel to the polarization direction. At submillimeter and millimeter wavelengths, the dust grains emit polarized radiation and the inferred magnetic field is orthogonal to the polarization direction. See Lazarian (2007) for a review of the theory of magnetic dust grain alignment.

Because the outflow is larger and more easily observed than the pseudodisk, most tests for magnetic regulation of core-collapse have focused on measuring alignment between outflow axes and magnetic field directions. For example, Ménard & Duchêne (2004) found no correlation when they compared the axes of T-Tauri star outflows in the Taurus molecular cloud with magnetic field directions inferred from optical and near-IR polarimetry. Similarly, Targon et al. (2011) used protostars with a range of ages and also found no correlation between outflow axis and field direction. One possible conclusion from these studies is that circumstellar disks form with their axes oriented randomly with respect to the fields in the natal cores. An alternative possibility is that outflows from T-Tauri stars will have injected more turbulence into their surroundings, in comparison with outflows from the much younger Class 0 sources. This additional turbulence could scramble any initial alignment between the disk/outflow system and the core magnetic field. Indeed, when Targon et al. (2011) focused on just the Class 0 and Class I sources in their sample, they did find a statistical alignment between outflow axis and magnetic field direction. Observations of polarized dust emission at 850 $\mu$m in Bok globules have found the magnetic field to be nearly aligned with the outflow axis or pseudodisk symmetry axis in some sources, but in other sources the field is closer to being perpendicular to the outflow axis (e.g., Henning et al. 2001; Vallée et al. 2003; Wolf et al. 2003). High resolution interferometric submillimeter polarimetry of NGC 1333 IRAS 4A has revealed the first clear case of a pinch morphology in a low-mass star-forming core (Girart et al. 2006). The symmetry axis of the pinched magnetic field was found to be nearly aligned with the minor axis of the inner core. Subsequently, Attard et al. (2009) mapped the magnetic field in this core on larger spatial scales and found a fairly uniform field running parallel to the symmetry axis of the small-scale hourglass field.

As illustrated by these examples, previous work has found some cases of alignment between magnetic fields and outflows or magnetic fields and pseudodisks, but a number of counter examples as well. However, the variety of evolutionary stages, stellar masses, stellar multiplicities, and spatial scales probed in these studies confuses comparisons with core-collapse models. To address these shortcomings, we began a submillimeter polarimetric survey of low-mass, isolated (i.e. single), nearby ($\lesssim$ 400 pc), young (Class 0) YSOs with well-defined bipolar outflows. Furthermore, we attempted to include only YSOs whose outflows lie nearly parallel to the plane of the sky, although we were not always successful in this regard, as discussed later in this section. Our source selection criteria aim to ensure that the objects in our sample have simple geometries that are not confused by nearby objects and are close enough that we can resolve small size scales ($\leq$ 4000 AU) in the centers of cores. Thus, our survey is providing data for direct comparison with magnetically regulated core-collapse models. The first paper from this survey presented results for B335, L1527, and IC348-SMM2 (Davidson et al. 2011, hereafter Paper I). These three cores exhibit flattened central regions consistent with their being edge-on pseudodisks. The symmetry axis of the pseudodisk in each core is nearly parallel to the outflow axis. The magnetic fields in cores show some degree of agreement with the predictions of magnetically regulated core-collapse models, but Paper I concluded that more data were needed for definitive tests.

In the present paper we expand the survey by presenting results for four new sources: L483, L1157, L1448-IRS2, and Serp-FIR1. In § 2 we discuss the observations and the data reduction, and we present our measurements. In § 3 we show the inferred magnetic field maps for each of the four cores, and we provide information (compiled from the literature) concerning bipolar outflows and pseudodisk-like structures in the cores. Despite our best efforts in choosing sources, recent work suggests that Serp-FIR1 has its outflow aligned nearly parallel to the line-of-sight (Enoch et al. 2009). For the other three cores, just as for the cores in Paper I, the outflows are much less inclined with respect to the plane of the sky (estimated inclination angles never exceed 40°). In § 4 we present a combined analysis of our current survey sample of seven cores, including four from the present paper and three from Paper I. We test for the predicted alignment between core magnetic field direction and pseudodisk symmetry axis, and we also test for a correlation between core magnetic field direction and outflow axis. In addition, to increase the signal-to-noise ratio we create a source-averaged magnetic field map by combining measurements from multiple sources. These

**Table 1**
SHARP 350 $\mu$m Polarimetry Observations

| Source | Dates Observed | No. HWP Cycles | $\tau_{350\ \mu m}$[a] | Chop Throw[b] (arcsec) |
|---|---|---|---|---|
| L483 | 2009 Sept 20-22 | 34 | 1.3-1.8 | 300 |
| | 2010 Mar 27 | 13 | 0.8-0.9 | 300 |
| | 2010 June 2-3 | 11 | 0.8-1.3 | 180,300 |
| L1157 | 2008 Sept 6-10 | 136 | 0.6-1.5 | 300 |
| L1448-IRS2 | 2009 Sept 17,20-22 | 92 | 1.2-1.9 | 300 |
| | 2009 Nov 8 | 21 | 1.4-1.7 | 180 |
| Serp-FIR1 | 2009 Sept 21 | 5 | 1.3 | 300 |
| | 2010 June 4 | 11 | 1.8 | 300 |

[a] Zenith atmospheric opacity at 350 $\mu$m
[b] Chop distance in cross-elevation

analyses make use of previously published estimates of outflow inclination angle for each of our seven cores. In § 5 we discuss the implications of our results for understanding magnetic effects in star formation. Lastly, in § 6 we summarize our results.

## 2. OBSERVATIONS AND RESULTS

Polarimetric observations of L483, L1157, L1448-IRS2, and Serp-FIR1 were obtained using the SHARP polarimeter during five observing runs at the Caltech Submillimeter Observatory (CSO). The runs took place during the period September 2008–June 2010. SHARP (Li et al. 2008) is a fore-optics module that adds polarimetric capabilities to SHARC-II, a $12 \times 32$ pixel bolometer array used at the CSO (Dowell et al. 2003). SHARP separates the incident radiation into two orthogonal polarization states that are then imaged side-by-side on the SHARC-II array. SHARP includes a half-wave plate located upstream from the polarizing splitting optics. The wavelength of observation was 350 $\mu$m and the effective beam size was $\sim 10''$. Polarimetric observations with SHARP involve carrying out chop-nod photometry at each of four half-wave plate rotation angles; a single such cycle requires approximately seven minutes. Additional details concerning the observations are listed in Table 1.

A full discussion of our data acquisition and reduction procedures is given in Paper I. Here, however, we will go into some detail on the calculation of errors since this was done differently in the present paper than in Paper I. The Stokes parameters $I$, $Q$, and $U$ represent the total ($I$) and linearly polarized ($Q$, $U$) flux and are derived from the flux detected at each of the four HWP angles during a single cycle. For the analysis presented in Paper I, the authors divided the data into subsets and computed the reduced chi-squared, $\chi^2_r$, among them to check if the results were consistent within the nominal uncertainties. The $\chi^2_r$ values from that analysis ranged from 1.5 to 2.1, suggesting that the nominal errors were too small. The "extra errors" are caused by correlated noise between pixels (covariance). The errors were shown to occur on relatively short time scales, so they were treated as if they were statistical in nature, i.e. the nominal errors were inflated by the square root of $\chi^2_r$ to produce the final errors.

For the present paper we handled these extra errors by using the generalized Gauss-Markov theorem, which statistically accounts for the covariance between pixels (e.g., Cox et al. 2006). In addition to computing the variance of each pixel in the Stokes parameter maps for a given cycle, we also calculated the covariance between each pair of pixels. When the single-cycle Stokes parameter maps for a core were combined to create the final Stokes parameter maps, the generalized Gauss-Markov theorem was used to propagate the variances and covariances and compute the final uncertainties for each pixel. By including the covariances in this way, the resulting uncertainties became larger. However, the reduced chi-squared values computed during consistency checking became smaller. Specifically, our $\chi^2_r$ values were 1.04 (L483), 1.19 (L1157), 0.99 (L1448-IRS2), and 1.21 (Serp-FIR1). Since these reduced chi-squared values were near unity, there was no reason to inflate our nominal errors. The net result of our new covariance analysis method is that the final signal-to-noise is mostly unaffected compared to the older chi-squared inflation method. However, the processing is more straightforward.

Our combined Stokes parameter maps contain polarization measurements for every $9\farcs5$ grid point. The grid is centered at the position of the source's peak flux. These Stokes parameters were converted to percentage polarization ($p$) and polarization angle ($\theta$). Since polarization cannot be negative, this leads to a small positive polarization bias, for which we corrected (Hildebrand et al. 2000; see also Vaillancourt 2006). We considered any polarization measurement having $p/\sigma_p \geq 2$ after debiasing to be a detection. Our polarization detections are listed in Table 2. Note that our cutoff is at $2\sigma$, rather than a more traditional (and conservative) $3\sigma$ threshold. With a $2\sigma$ threshold, the uncertainties in polarization angle range up to almost 13°. However, because we are only testing the gross predictions of magnetically regulated core-collapse models, this cutoff level is acceptable.

## 3. POLARIZATION MAPS FOR INDIVIDUAL SOURCES

In this section we will compare our submillimeter polarization data with the observed outflow direction, pseudodisk position angle, and the predictions of the magnetically regulated core-collapse model of Allen et al. (2003a, hereafter ALS03), just as was done in Paper I. The ALS03 model numerically computes the gravitational collapse of a singular isothermal core that is magnetized and rotating with its rotation axis aligned with the large-scale magnetic field. To compare our SHARP data with this model, we need the pseudodisk position angle and

**Table 2**
SHARP 350 $\mu$m Polarimetry Results

| Source | $\Delta\alpha$[a] ($''$) | $\Delta\delta$[a] ($''$) | $p$ (%) | $\sigma_p$ (%) | $\theta$[b] (deg) | $\sigma_\theta$[b] (deg) | I[c] (%) |
|---|---|---|---|---|---|---|---|
| L483 | 19.0 | -28.5 | 17.4 | 7.9 | 27.6 | 10.2 | 14 |
| | 19.0 | -19.0 | 9.3 | 4.1 | 5.7 | 10.9 | 17 |
| | 9.5 | -19.0 | 5.7 | 2.2 | 12.8 | 10.1 | 20 |
| | 9.5 | 0.0 | 1.0 | 0.5 | -7.4 | 12.7 | 78 |
| | 0.0 | 19.0 | 4.6 | 1.5 | 41.6 | 8.6 | 29 |
| | -9.5 | 0.0 | 0.8 | 0.4 | 5.7 | 12.4 | 71 |
| | -19.0 | -19.0 | 3.5 | 1.3 | -1.8 | 9.9 | 27 |
| | -19.0 | -9.5 | 1.7 | 0.7 | -13.5 | 11.6 | 41 |
| | -28.5 | -19.0 | 6.0 | 2.3 | -23.2 | 10.0 | 20 |
| | -38.0 | 0.0 | 7.5 | 3.5 | -19.2 | 11.7 | 17 |
| L1157 | 19.0 | -19.0 | 7.4 | 3.5 | -85.2 | 10.4 | 11 |
| | 0.0 | 0.0 | 0.7 | 0.2 | 52.1 | 9.0 | 100 |
| | -9.5 | 19.0 | 5.8 | 2.5 | 40.1 | 10.6 | 11 |
| | -19.0 | 9.5 | 5.4 | 2.6 | 41.5 | 12.0 | 11 |
| L1448 IRS2 | 38.0 | -9.5 | 9.5 | 3.2 | 61.2 | 9.0 | 31 |
| | 38.0 | 0.0 | 9.5 | 3.2 | 34.8 | 8.7 | 29 |
| | 28.5 | -19.0 | 9.6 | 3.3 | 63.5 | 8.9 | 23 |
| | 19.0 | 0.0 | 4.0 | 1.5 | 50.2 | 10.1 | 31 |
| | 9.5 | -38.0 | 14.5 | 5.8 | 74.4 | 9.7 | 20 |
| | 9.5 | -28.5 | 7.5 | 2.7 | 75.1 | 9.6 | 25 |
| | 9.5 | 0.0 | 2.2 | 0.8 | 50.4 | 9.7 | 53 |
| | 9.5 | 9.5 | 2.5 | 1.2 | 51.4 | 12.2 | 38 |
| | 9.5 | 19.0 | 7.6 | 2.9 | 56.1 | 10.1 | 19 |
| | -9.5 | 19.0 | 9.6 | 3.9 | 73.8 | 10.4 | 16 |
| | -19.0 | -28.5 | 7.5 | 3.5 | 74.1 | 12.2 | 21 |
| | -19.0 | -9.5 | 4.9 | 2.3 | 55.9 | 12.0 | 23 |
| | -19.0 | 9.5 | 7.3 | 3.4 | 65.4 | 11.9 | 18 |
| Serp FIR1 | 19.0 | -9.5 | 5.1 | 1.7 | 7.1 | 8.2 | 18 |
| | 9.5 | -19.0 | 3.5 | 1.4 | 2.8 | 10.1 | 19 |
| | 0.0 | -38.0 | 14.8 | 7.1 | 12.6 | 9.3 | 8 |
| | 0.0 | 9.5 | 1.0 | 0.4 | -22.7 | 10.0 | 46 |
| | -9.5 | -9.5 | 1.6 | 0.8 | -30.1 | 12.0 | 25 |
| | -9.5 | 0.0 | 1.2 | 0.4 | -31.2 | 8.9 | 41 |
| | -19.0 | -19.0 | 3.7 | 1.7 | -2.2 | 11.4 | 13 |
| | -19.0 | -9.5 | 3.3 | 1.2 | -44.2 | 9.1 | 15 |
| | -19.0 | 0.0 | 2.3 | 1.1 | -45.2 | 12.4 | 15 |
| | -28.5 | -19.0 | 6.9 | 3.2 | 14.5 | 10.8 | 9 |

[a] Offsets in arcseconds from positions listed in Table 3
[b] Position angle of the polarization $E$-vector, measured east of north
[c] Intensity as a percentage of the peak for each core

core infall radius for each source. Using the literature, we compiled these and other relevant properties for each source and we list them in Table 3. We give a detailed discussion of how the information in Table 3 was obtained in § 3.2 through § 3.5.

### 3.1. *Overview of Polarization Maps*

The red and blue lines (vectors) in Figures 1 through 4 show the inferred magnetic field directions for each core in a manner similar to Figures 2 through 7 in Paper I. These inferred field directions are orthogonal to the measured directions of the 350 $\mu$m polarization. In the left panel, the vectors are plotted with lengths proportional to the percentage polarization. As in Paper I, we distinguish between high-flux and low-flux regions as a way to flag polarization measurements that may have large contamination from the parent cloud. Red vectors are used for sight-lines where the flux is greater than or equal to 25% of the peak flux, while blue vectors indicate sight-lines not meeting this threshold. The 25% flux cutoff matches the level used in Paper I.

The left panel of each figure shows in grayscale a *Spitzer* 4.5 $\mu$m waveband image. This waveband is an excellent tracer of outflows because it contains a shocked $H_2$ emission line. For L483 and Serp-FIR1, images are from the final delivery of the *Cores to Disks* Legacy Science program[14] while for L1157 and L1448-IRS2 images are from the *Spitzer* Heritage Archive[15]. Overlaid on each *Spitzer* image are contours of the observed 350 $\mu$m emission, ranging from 20% to 90% of the peak flux in steps of 10%. The dashed circle and double-headed black vector indicate the infall radius and outflow position angle for each source, respectively (estimated from observations, see Table 3). The right panel plots the inferred magnetic field vectors superposed on Figure 8(c) from ALS03. Each vector is now shown with the same length to make the magnetic field morphology clearer. The vector locations are scaled to the model infall radius and the model is rotated by the pseudodisk position angle. It is important to note that there are no free parameters to help fit the magnetic field vectors to the ALS03 model. The infall radius and pseudodisk position angle are set by observations.

Also shown in each figure is the mean magnetic field direction that we computed for each core (white outlined double-headed arrow). In Paper I this mean was not computed, but we require it for the statistical analyses that we will carry out in § 4.2 below. Because a polarization angle of 0° is the same as 180°, computing the mean polarization angle is non-trivial. We use the Equal Weight Stokes Mean, defined by Li et al. (2006). In brief, this method converts each angle to Stokes $q = Q/I$ and $u = U/I$, computes the unweighted averages $\bar{q}$ and $\bar{u}$, and then converts $\bar{q}$ and $\bar{u}$ back to an angle. The uncertainty in mean angle is derived from propagation of errors. Only the red vectors in each core are used when computing the mean magnetic field angle.

ALS03 present several models corresponding to different values of magnetic field strength and rotation speed. Just as in Paper I, we show only one model, corresponding to Fig. 8(c) of ALS03, chosen because it has intermediate values for both magnetization and rotation. However, note that all models in ALS03 (excluding the unmagnetized one) show a similar pinch in the field. Data from our survey cannot yet resolve the small differences between the various models in ALS03. Also, it is important to keep in mind that ALS03 display a slice through the center of their core. Averaging of the magnetic field along the line-of-sight will lessen the observed pinch in the field. Furthermore, large inclination angles of the pseudodisk symmetry axis will distort the observed pinch pattern. ALS03 show this distortion in their Figure 4 for inclinations of 30° and 90°. At an inclination of 30° the distortion is mild, but at 90° the magnetic field lines extend radially outwards from the core center, with some twisting due to rotation.

### 3.2. *L483*

L483 is located in the Aquila Rift at a distance of $200 \pm 30$ pc (Prato et al. 2008). The embedded protostar in L483 is IRAS 18148-0440. Based on its spectral energy distribution, it is usually classified as a Class 0 protostar (Fuller et al. 1995). However, Tafalla et al. (2000) argued that the outflow from the protostar shares some

[14] http://irsa.ipac.caltech.edu/data/SPITZER/docs/spitzermission/observingprograms/legacy/c2d/
[15] http://archive.spitzer.caltech.edu/

**Table 3**
Basic Source Properties

| Information | L483 | L1157 | L1448-IRS2 | Serp-FIR1 |
|---|---|---|---|---|
| Right Ascension (J2000) | 18 17 29.8[(1)] | 20 39 06.2[(6)] | 03 25 22.3[(6)] | 18 29 49.6[(16)] |
| Declination (J2000) | -04 39 38.3[(1)] | 68 02 15.9[(6)] | 30 45 13.3[(6)] | 01 15 21.9[(16)] |
| Distance (pc) | $200 \pm 30$[(2)] | $325 \pm 13$[(7)] | $232 \pm 18$[(12)] | $415 \pm 5$[(17)] |
| Pseudo-disk P.A. (deg)[a] | 36[(3)] | 75[(8)] | 45[(6,13)] | ... |
| Infall Radius (AU) | 8000[(4)] | 8500[(9)] | 8000[(14)] | 5000[(18)] |
| Outflow Properties | | | | |
| Position Angle (deg)[a] | 105[(5)] | 155[(10)] | 138[(15)] | 130[(19)] |
| Inclination Angle (deg)[b] | $40 \pm 10$[(5)] | 9[(11)] | $33 \pm^{8}_{6}$[(14)] | $72.5 \pm 7.5$[(18)] |

**References**. — (1) Jørgensen (2004); (2) Prato et al. (2008); (3) Fuller & Wootten (2000); (4) Myers et al. (1995); (5) Fuller et al. (1995); (6) Kwon et al. (2009); (7) Straizys et al. (1992); (8) Looney et al. (2007); (9) Gueth et al. (1997); (10) Davis & Eisloeffel (1995); (11) Gueth et al. (1996); (12) Hirota et al. (2011); (13) Chen et al. (2010); (14) Tobin et al. (2007); (15) Davis et al. (2008); (16) Harvey et al. (2007); (17) Dzib et al. (2010); (18) Enoch et al. (2009); (19) Rodriguez et al. (1989)

[a] Position angles denote the angle of the long axis of the pseudodisk or outflow, measured east of north.
[b] The inclination angle is measured with respect to the plane of the sky.

properties with those observed in more evolved sources and that IRAS 18148-0440 may thus be transitioning from Class 0 to Class I.

The inclination angle of the outflow in L483 is not well-known. In the present paper we measure inclination from the plane of the sky; thus 0° inclination means the outflow is parallel to the sky plane and 90° means the outflow is pointing along the line-of-sight. Fuller et al. (1995) measured differences in 2.22 $\mu$m brightness between the eastern and western lobes of the outflow. By fitting this emission to a simple model, they estimated the inclination angle to be 40°. Based on their Figure 5 we estimate an uncertainty of ±10° on the inclination. This 40° inclination is the only quantitative value for the inclination angle in the literature, but it may be an overestimate. Hatchell et al. (1999) measured $^{12}$CO $J = 4 \rightarrow 3$ emission from the outflow and found some overlap between the red- and blue-shifted emission in each outflow lobe, which suggests that the L483 outflow has a smaller inclination angle. We estimate the position angle of the outflow to be 105° based on the shocked $H_2$ emission (Fuller et al. 1995).

There are no molecular line measurements of a pseudodisk in L483. This could be due to depletion and possibly also optical depth effects (Fuller & Wootten 2000; Park et al. 2000; Jørgensen 2004). Fuller & Wootten (2000) observed a narrow absorption lane at 3.4 $\mu$m with a width of ∼250 AU. From visual inspection of their Figure 4, we estimate that the diameter of this absorption lane must be ∼1000–2000 AU based on the apparent 3.4 $\mu$m extinction. The lane can also be seen at lower resolution in the *Spitzer* 4.5 $\mu$m emission in Figure 1. It has roughly the right size to be a pseudodisk. We measured its position angle to be 36°, which we adopt as the pseudodisk position angle.

There are two different estimates for the infall radius of L483. Myers et al. (1995) observed $N_2H^+$ and $C_3H_2$ rotational emission lines at the source peak and nearby positions offset from the peak. They found that the centroid line velocities decreased (suggesting infall motion) as positions approached the protostar over a distance of 0.04 pc (40″ for a 200 pc distance). Tafalla et al. (2000) detected self-absorption in the $H_2CO$ ($2_{12}-1_{11}$) emission toward L483, with a brighter blue-shifted peak compared to the red-shifted peak, indicative of infall motions. The radius over which they were able to measure a stronger blue-shifted peak was 20″. Because the self-absorption profile requires specific physical conditions to occur, the lack of a stronger blue-shifted peak is not necessarily evidence for lack of infall. Therefore, we adopt an infall radius of 40″ for this paper.

Figure 1 shows the inferred magnetic field in L483. The 20% contour of the 350 $\mu$m emission appears distorted due to artifacts at the edge of the map. The magnetic field is fairly ordered with a mean direction of $93 \pm 6°$. The mean field direction is offset by 12° from the direction of the outflow and offset by 33° from the symmetry axis of the pseudodisk. Considering the red and blue vectors together, there is a suggestion of a pinch in the magnetic field.

Dotson et al. (2010) reported polarimetric observations of L483 at 350 $\mu$m. They obtained several upper limits ($p + 2\sigma_p < 1\%$) for sight lines near the flux peak and three polarization detections from the periphery (regions with $I \lesssim 20\%$ of their peak flux). Our two vectors closest to the flux peak have polarization magnitudes of 1.0% and 0.8%, consistent with the upper limits of Dotson et al. (2010). Only one of the periphery vectors from Dotson et al. (2010) overlaps regions where we detect polarization; this occurs at $(\Delta RA, \Delta DEC) \sim (+30'', -20'')$. We detect polarization at two locations near this position. Taken together, and considering the coarser angular resolution of Dotson et al. (2010), our vectors agree with their measurement in both polarization angle and polarization percentage.

### 3.3. *L1157*

The first distance estimate for L1157 was 440 pc, based on the distance to the NGC 7023 open cluster (Viotti 1969). More recently, Kun (1998) estimated distances of 200, 300, and 450 pc for different clouds in Cepheus. Because the Galactic latitude of L1157

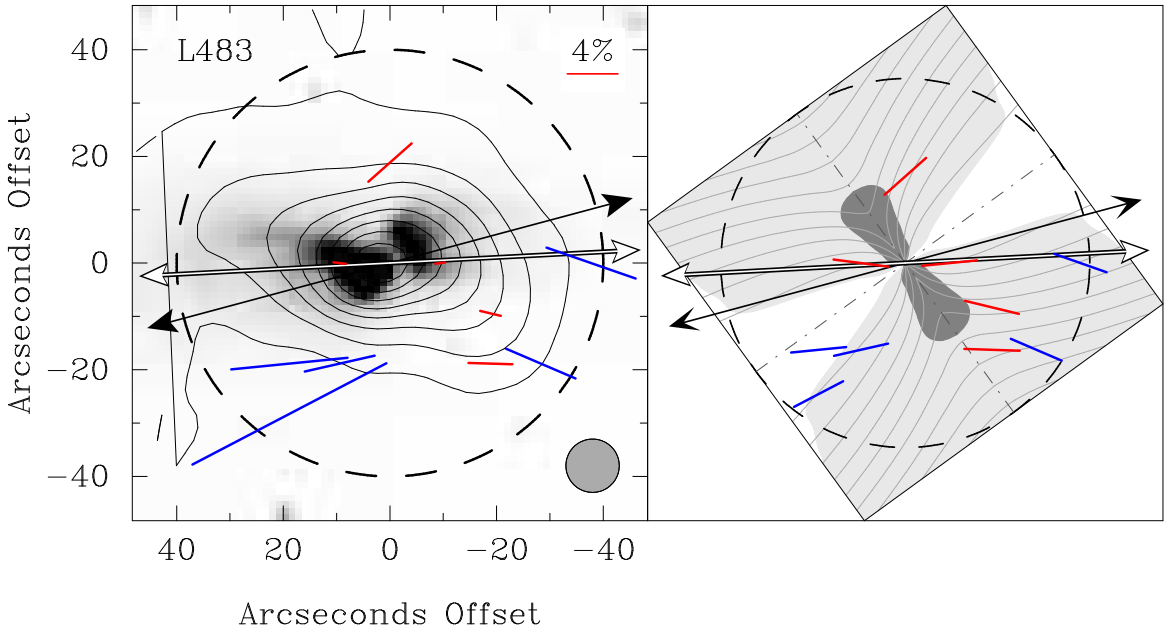


**Figure 1.** Inferred magnetic field direction for the core L483. *(left)* The halftone image shows the *Spitzer* IRAC band 2 (4.5 $\mu$m) emission for the core. Contours show the 350 $\mu$m intensity; they range from 20% to 90% of the peak flux, in steps of 10%. Red and blue vectors show the measured 350 $\mu$m polarization, where the angle of each vector has been rotated by 90° to show the inferred magnetic field direction. Vectors are plotted for points where $p/\sigma_p \geq 2$ after debiasing. The length of each vector has been scaled in proportion to its percentage polarization. Red vectors indicate positions where the flux is greater than or equal to 25% of the peak flux, blue vectors indicate positions not meeting this threshold. The large black vector shows the outflow direction, while the white outlined vector is the mean magnetic field direction computed from the red vectors. The dashed circle indicates the measured infall radius. The gray circle at the bottom right shows the SHARP beam size (10″). *(right)* The magnetic field vectors plotted on the core-collapse infall model taken from Figure 8(c) of Allen et al. (2003a). All vectors have been plotted the same length. The dark grey region shows the model pseudodisk. The grey lines show the model magnetic field lines. The dashed-dotted lines are the orientation axes for the model pseudodisk. The model has been rotated to match the measured position angle of the observed pseudodisk.

is similar to that of the 200 pc and 300 pc clouds, some recent authors have assumed a distance of 250 pc for L1157 (Looney et al. 2007; Chiang et al. 2010; Tobin et al. 2010). Straizys et al. (1992) used an interstellar reddening-distance relationship to estimate a distance of 325 ± 13 pc for the L1147/L1158 subgroup (which includes L1157). The latter distance was used by the *Spitzer* Gould's Belt Legacy Science Program (Kirk et al. 2009) and is the distance we adopt here. L1157 contains the Class 0 protostar IRAS 20386+6751 (Gueth et al. 1997).

The outflow in L1157 has an inclination angle of 9° (Gueth et al. 1996). It has been mapped in shocked $H_2$ by Davis & Eisloeffel (1995) who found a position angle of 155°. L1157 has a flattened envelope roughly perpendicular to the outflow. It is very prominent in 8 $\mu$m absorption with a diameter of ∼2′ (Looney et al. 2007). Chiang et al. (2010) observed $N_2H^+$ $J = 1 \rightarrow 0$ and found it to spatially coincide with the absorption feature. The full width half-maximum of the $N_2H^+$ is ∼11″×18″, or ∼3600×5900 AU at the distance of L1157. The $N_2H^+$ emission shows evidence of both infall and rotation (Chiang et al. 2010) and its size is not too different from the predicted pseudodisk size, so we adopt the position angle of the $N_2H^+$ emission, which is 75°, as the pseudodisk position angle. Gueth et al. (1997) observed $^{13}$CO $J = 1 \rightarrow 0$ and $J = 2 \rightarrow 1$ transitions in L1157. Both spectra show a self-absorption profile with the blue-shifted peak stronger than the red-shifted peak, indicating infall (see their Figure 8). Using these two spectra, Gueth et al. (1997) estimated the path length towards the central protostar of the $^{13}$CO to be 8500 AU. We adopt this value as the infall radius for L1157.

We show our results for L1157 in Figure 2. Only one of our polarization detections has a corresponding flux value greater than or equal to 25% of the flux peak. This vector appears at the peak and has $> 3\sigma$ significance. It is offset by 13° with respect to the outflow axis and by 23° with respect to the pseudodisk symmetry axis. Hull et al. (2013) measured 1.3 mm polarization in L1157 on spatial scales much smaller than those studied in the present paper. Their mean magnetic field is consistent with our measurement, and will be discussed in more detail in § 5.

### 3.4. *L1448-IRS2*

The L1448 complex is located in the Perseus cloud. L1448-IRS2 lies approximately 3′ west of L1448-mm/L1448C and L1448-IRS3 and 3′ east of L1448-IRS1. In addition, roughly 50″ east of IRS2 is a candidate first hydrostatic core labeled L1448-IRS2E (Chen et al. 2010). Hirota et al. (2011) obtained a distance of 232 ± 18 pc towards $H_2O$ masers in L1448C. Because of L1448C's proximity, we adopt this distance for L1448-IRS2. L1448-IRS2 contains the protostar IRAS 03222+3034. Based on its spectral energy distribution it is a Class 0 source (O'Linger et al. 1999).

The position angle for the outflow is 138° as derived from shocked $H_2$ emission (Davis et al. 2008). Less certain is the inclination angle of the outflow. Tobin et al. (2007) used radiative transfer codes (Whitney et al. 2003a,b) to model continuum emission data covering the

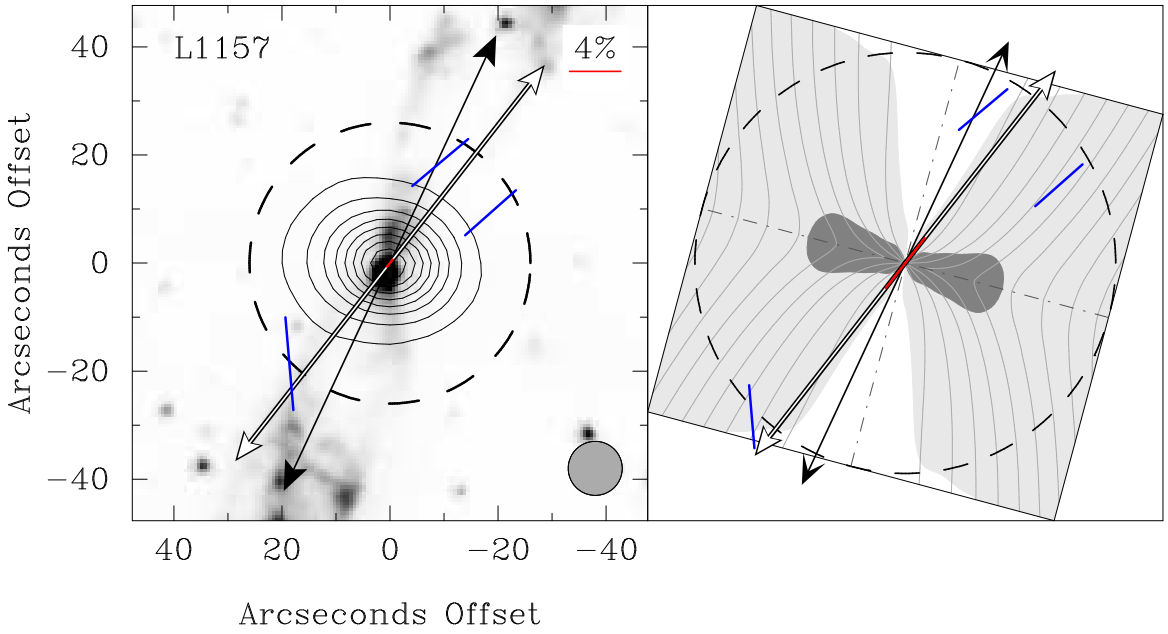


**Figure 2.** Same as Figure 1, except for L1157.

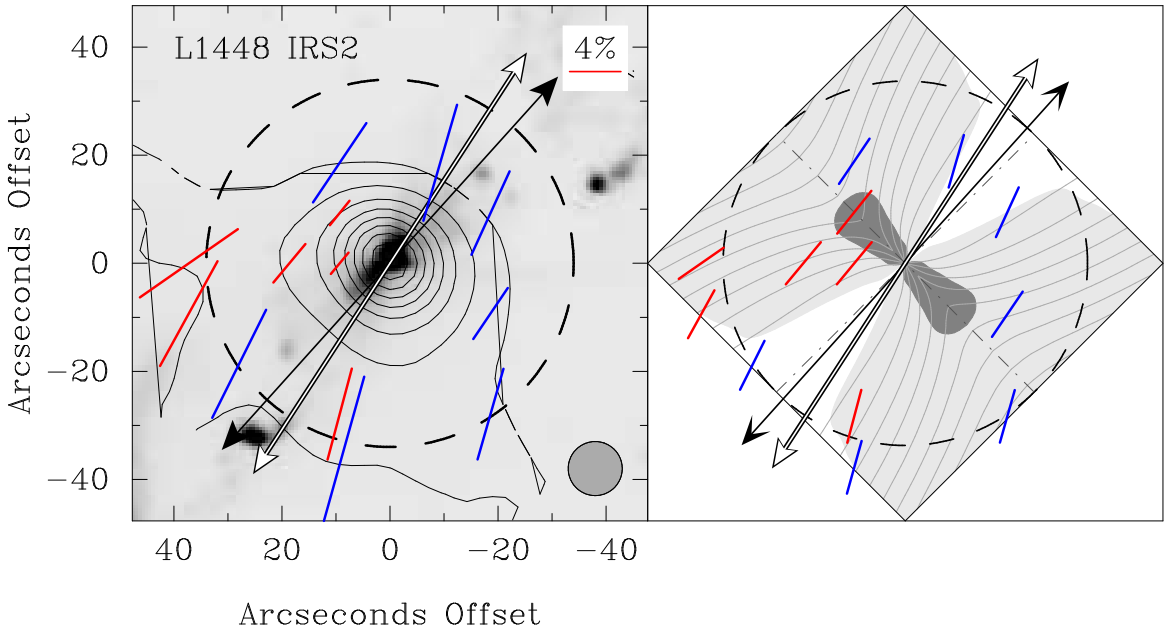


**Figure 3.** Same as Figure 1 except for L1448-IRS2. The two easternmost red vectors are excluded when computing the mean field direction. See § 3.4 for details.

wavelength range 2.2 $\mu$m to 2.7 mm. The best fit inclination angle is $33^{+8}_{-6}$ degrees. A possible pseudodisk has been observed in 1.3 mm continuum emission by both Kwon et al. (2009) and Chen et al. (2010) with 5″ and 3″ resolution, respectively. In both maps, the core appears extended with a long axis oriented at position angle 45°. We measure the length of the long axis as ∼14″ from the data of Kwon et al. (2009) and ∼5″ from the data of Chen et al. (2010). Thus the spatial size is ∼1000–3000 AU for a distance of 232 pc. There are no direct measurements of the infall radius for this source. However, the best-fit model from Tobin et al. (2007) has an envelope radius of 8000 AU. Because the Whitney et al. (2003a,b) models use an infalling envelope, we adopt the envelope radius as the infall radius for L1448-IRS2.

In Figure 3 we plot our results for L1448-IRS2. We pick up some emission from L1448-IRS2E at the edges of our map. This emission is the primary reason for the distorted 20% contour. Taken together, the red and blue vectors are very ordered with a uniform direction. There is no evidence of a pinch in the magnetic field. Note that the two easternmost vectors arise from the wings of L1448-IRS2E. To avoid any possible bias, we exclude these vectors and use only the remaining four red vectors in computing the mean field direction. The mean field direction is $147 \pm 5°$ which is offset by 9° from the outflow axis and by 12° from the pseudodisk symmetry axis. Hull et al. (2013) measured 1.3 mm polarization

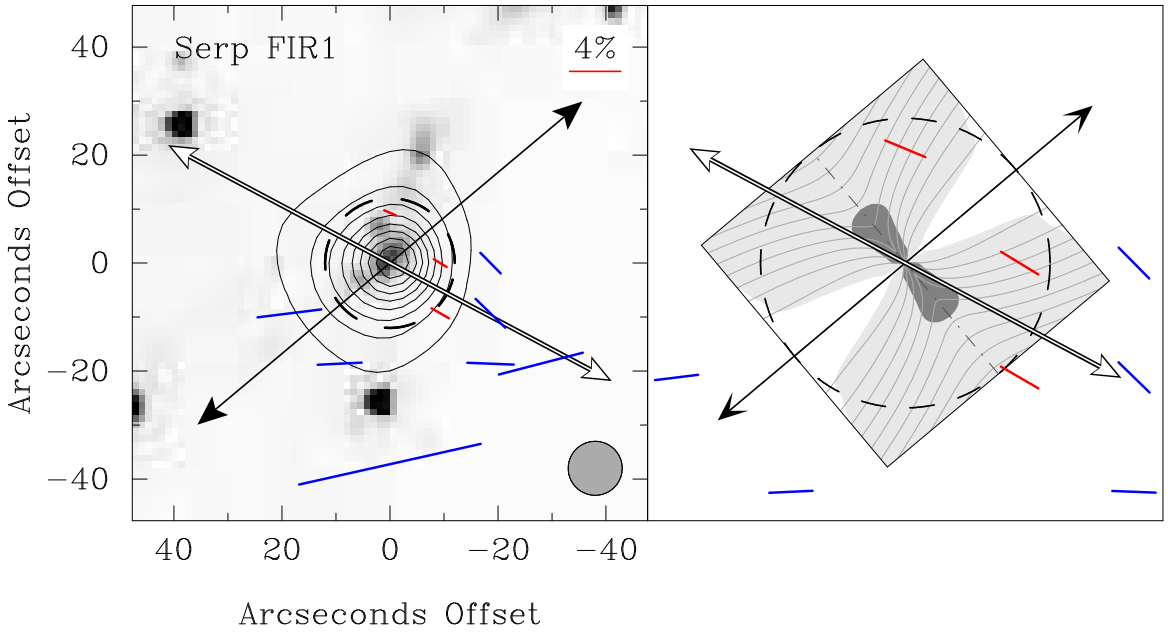


**Figure 4.** Same as Figure 1 except for Serp-FIR1. Because no pseudodisk has been found for this source, the model in the right panel was rotationally aligned with the observed outflow axis. Note that the outflow in this source is nearly parallel to the line-of-sight.

in L1448-IRS2 on spatial scales much smaller than those studied in the present paper. Their mean magnetic field is consistent with our measurement, and will be discussed in more detail in § 5.

### 3.5. *Serp-FIR1*

Serp-FIR1 (also known as Serp-SMM1) is located in the Serpens core. Most distance estimates for Serpens are in the range 200–400 pc (Eiroa et al. 2008). In the present paper we adopt a distance of $415 \pm 5$ pc based on the work of Dzib et al. (2010), who measured the trigonometric parallax for the binary YSO EC95, located in the Serpens cloud core. Serp-FIR1 is the brightest source in the Serpens core at submillimeter wavelengths and contains the Class 0 protostar IRAS 18273+0113 (Hurt & Barsony 1996).

The Serp-FIR1 outflow has been observed in 6 cm continuum with the Very Large Array. The continuum is resolved into three peaks, one centered on the source, the other two offset by $\sim 6''$ on either side (Rodriguez et al. 1989). The three peaks form a straight line with a position angle of 130°. The inclination angle of the outflow is not well-determined. Enoch et al. (2009) performed radiative transfer modeling of continuum emission in multiple wavebands from 3.6 $\mu$m to 1 mm. Their best-fit inclination angle for the outflow is 75°, although angles in the range 65°–80° also produce reasonable fits. We adopt an inclination angle of $72.5 \pm 7.5°$. No candidate pseudodisk has been observed for Serp-FIR1. High-resolution interferometric observations show a very round or unresolved core at 3 mm (Williams & Myers 2000; Hogerheijde et al. 1999; Enoch et al. 2009) and also at 1 mm (Hogerheijde et al. 1999; Enoch et al. 2009). If the pseudodisk axis is close to the outflow axis (see § 4.1), then this could be a projection effect; a flattened envelope would appear round if viewed face-on. There are no measurements of an infall radius for Serp-FIR1. Because the model from Enoch et al. (2009) is of a rotating, collapsing sphere, we adopt their best-fit envelope radius of 5,000 AU.

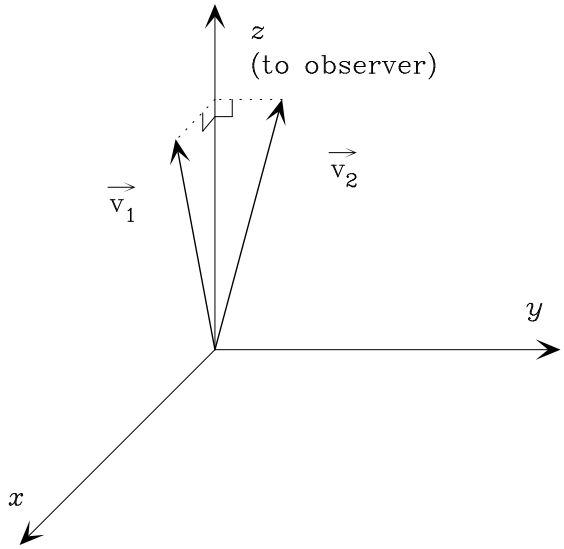


**Figure 5.** Cartoon showing how viewing angle can alter the projected separation between two vectors. $\vec{v}_1$ lies in the $xz$ plane and $\vec{v}_2$ lies in the $yz$ plane. To an observer looking along the $z$ axis, the projected separation angle between the two vectors is 90°, even though their true separation angle is 21°.

Our results for Serp-FIR1 are shown in Figure 4. Despite the high inclination angle for the Serp-FIR1 outflow, for completeness we plot the vectors on the ALS03 model in Figure 4. The position angle of the pseudodisk plane is taken to be perpendicular to the outflow axis since no pseudodisk is detected (see discussion in § 4.1). The magnetic field is well-ordered. Its mean direction is 62±5°, nearly perpendicular to the outflow axis, and thus also to the assumed pseudodisk symmetry axis. This may indicate that magnetic fields do not regulate star formation in this core. Alternatively, it may be a projection effect caused by the outflow pointing nearly parallel to

**Table 4**
Source Properties Used For Combining Results

| Source | No. of Vectors | Mean $B$[a] (deg) | $\phi$[b] (deg) | Inclination[c] (deg) | Pixel Scale[d] (Infall Radius) |
|---|---|---|---|---|---|
| B335 | 1 | $149 \pm 15$ | $39 \pm 15$ | $9 \pm 1$ | 0.288 |
| IC348-SMM2 | 8 | $137 \pm 5$ | $9 \pm 5$ | $10 \pm 5$ | 0.380 |
| L1157 | 1 | $142 \pm 9$ | $23 \pm 9$ | $9 \pm 5$ | 0.363 |
| L1448-IRS2 | 4 | $147 \pm 5$ | $12 \pm 5$ | $33 \pm 7$ | 0.276 |
| L1527 | 9 | $49 \pm 4$ | $41 \pm 4$ | $7 \pm 1$ | 0.250 |
| L483 | 5 | $93 \pm 6$ | $33 \pm 6$ | $40 \pm 10$ | 0.238 |
| Serp-FIR1 | 3 | $62 \pm 5$ | $68 \pm 5$ | $72.5 \pm 7.5$ | 0.788 |

[a] Mean magnetic field position angle derived from SHARP data in the present paper and Paper I. See § 3.1 for details.
[b] Difference between the mean magnetic field position angle and the pseudodisk apparent minor axis. For Serp-FIR1, the outflow axis serves as a proxy for the pseudodisk minor axis.
[c] Inclination angle of outflow
[d] Size of a single pixel of the final Stokes parameter maps as a fraction of the infall radius.

the line-of-sight. To understand this, note that the perceived angle between two vectors is heavily dependent on viewing angle. This can be readily seen by considering the situation depicted in Figure 5. An observer along the $z$ axis will measure the projected separation angle between the two vectors to be 90°, even though the true angle between them is much smaller. We conclude that the high inclination of the Serp-FIR1 outflow makes this source a poor test of the basic predictions of magnetically regulated core-collapse (see § 1). We will further explore the effects of viewing angle on projected separation in § 4.2.

Polarization towards Serp-FIR1 has been detected at 850 $\mu$m by Matthews et al. (2009). In general, their polarization measurements trace the magnetic field in the cloud rather than in the Serp-FIR1 core. All but one of their vectors correspond to regions where the measured 350 $\mu$m flux is less than 20% of the peak flux. This one vector implies a magnetic field position angle of 63.3°, almost identical to our mean field direction. Hull et al. (2013) measured 1.3 mm polarization in Serp-FIR1 on spatial scales much smaller than those studied in the present paper. Their mean magnetic field direction differs by nearly 90° from our own. This will be discussed in more detail in § 5.

## 4. COMBINED ANALYSIS OF SEVEN CORES

In this section we will combine results for the four sources discussed in § 3 together with results for the three sources from Paper I (B335, IC348-SMM2, and L1527). We will compare results obtained from this combined sample of seven cores observed with SHARP with the predictions of magnetically regulated core-collapse models. We will need several additional pieces of information to carry out these comparisons; these are given in Table 4. For B335, IC348-SMM2, and L1527 we computed mean magnetic field position angles from the data in Table 1 of Paper I, using the method described in § 3.1 of the present paper. We obtained corresponding pseudodisk position angles from § 3.1 of Paper I, and corresponding outflow inclination angles from Table 2 of Paper I or from the literature. For B335 we used an outflow inclination $i = 9 \pm 1°$ (Moriarty-Schieven & Snell 1989) and for L1527 we used $i = 7 \pm 1°$ (Zhou et al. 1996). The inclination angles for two of the sources, IC348-SMM2 and L1157, do not have uncertainties in the literature. For these we used the average of the uncertainties in inclination on the other five cores, which was 5°.

Paper I used both SHARP 350 $\mu$m and SCU-POL 850 $\mu$m polarization data when analyzing the source B335. In the present paper we will only use the 350 $\mu$m data. With a total of seven cores, our survey now has a sufficiently large sample for us to be able to rely exclusively on the SHARP data, providing a homogeneous dataset. Emission at 850 $\mu$m traces cooler dust in comparison with 350 $\mu$m emission. For example, the ratio of 350 $\mu$m to 850 $\mu$m flux is three times larger for 20 K dust than it is for 10 K dust. Thus, the 350 $\mu$m polarization data preferentially trace warmer regions closer to the protostar while the 850 $\mu$m polarization data preferentially trace cooler regions further away from the central source.

### 4.1. *Correlation Between Outflow Axis and Pseudodisk Symmetry Axis*

We find a strong correlation between the projected outflow axis and the projected pseudodisk symmetry axis for all cores with a measured pseudodisk (i.e., all except Serp-FIR1). Using data from Table 3 of the present paper and Table 2 and § 3.1 of Paper I, we find that the differences in angle between these two axes are: 21° (L483), 10° (L1157), 3° (L1448-IRS2), 0° (L1527), 17° (IC348-SMM2), and 20° (B335). The mean of these six values is 12°. This tight correlation gives us confidence in using the outflow axis as a proxy for the pseudodisk symmetry axis in Serp-FIR1, as we did in § 3.5 above. In § 4.2 we will test for a correlation between the pseudodisk and magnetic field directions. For this purpose we will need the inclination of the pseudodisk axis. Because this is unknown, we will exploit the tight correlation between pseudodisk and outflow axes by using the inclination of a given source's outflow as a proxy for the inclination angle of that source's pseudodisk axis. Furthermore, for Serp-FIR1 (only) we will again use the position angle of the outflow as a proxy for the position angle of the pseudodisk axis, while for the remaining six sources we will use our measured pseudodisk axis position angles.

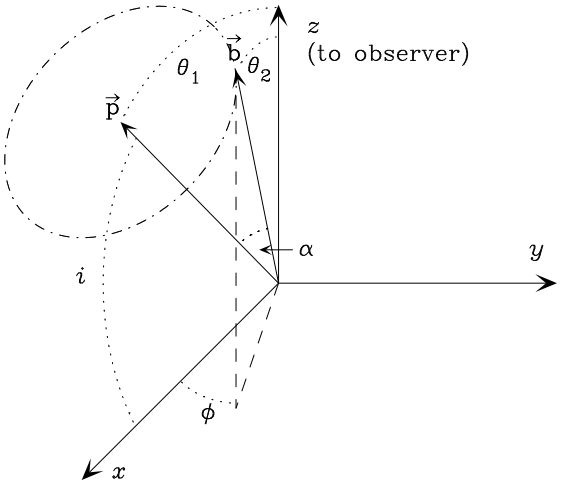


**Figure 6.** Cartoon showing the geometry for deriving the probability density function for the projected separation angle, $\phi$, between two vectors $\vec{p}$ and $\vec{b}$, as a function of the inclination $i$ of $\vec{p}$ and the intrinsic separation angle $\alpha$ between $\vec{p}$ and $\vec{b}$. Vector $\vec{p}$ represents the pseudodisk axis and is constrained to lie in the $xz$ plane, while vector $\vec{b}$ represents the average magnetic field direction. $\alpha$ and $i$ are held constant when computing the probability density function for $\phi$.

### 4.2. *Correlation Between Mean Magnetic Field and Pseudodisk Symmetry Axis*

We define $\phi$ to be the projected plane of sky separation angle between the mean magnetic field and the pseudodisk symmetry axis. The value of $\phi$ for each core is listed in Table 4. Since these values range from 9° to 68°, it appears that any correlation is much less evident than the correlation we found between outflow and pseudodisk axis. However, six of the seven $\phi$ values are less than 45°, and the remaining value corresponds to Serp-FIR1, which, as we discussed in § 3.5, has high outflow inclination making this source a poor test for intrinsic 3D alignment. In the remainder of this section, we will explore quantitatively a possible correlation between the 3D core magnetic field angle and the 3D pseudodisk symmetry axis for our sample of seven sources. We define $\alpha$ to be the true 3D separation angle between magnetic field and pseudodisk symmetry axis and $i$ to be the inclination angle of the pseudodisk symmetry axis. (Recall that we will use outflow inclination as a proxy for pseudodisk inclination, as discussed in § 4.1.) In our analysis, we assume that each source has the same $\alpha$, and we use our data to obtain a best estimate for this parameter.

Consider two vectors: $\vec{p}$, representing the pseudodisk symmetry axis, and $\vec{b}$, representing the mean magnetic field direction. Figure 6 shows the coordinate system and nomenclature used. Vectors $\vec{p}$ and $\vec{b}$ can be written in $xyz$ components as:

$$\vec{p} = p(\sin\theta_1,\ 0,\ \cos\theta_1) \tag{1}$$

$$\vec{b} = b(\sin\theta_2\cos\phi,\ \sin\theta_2\sin\phi,\ \cos\theta_2). \tag{2}$$

Now consider a new coordinate system that is rotated about the $y$ axis by $\theta_1$ degrees such that the new $z$-axis, which we call $z'$, is aligned with $\vec{p}$. Note that under this rotation $y' = y$. In the new $x'y'z'$ coordinate system $\vec{b}$ is written as:

$$\vec{b} = b(\cos\theta_1\sin\theta_2\cos\phi - \sin\theta_1\cos\theta_2,\ \sin\theta_2\sin\phi,\ \sin\theta_1\sin\theta_2\cos\phi + \cos\theta_1\cos\theta_2) \tag{3}$$

$$\equiv b(\sin\alpha\cos\phi',\ \sin\alpha\sin\phi',\ \cos\alpha), \tag{4}$$

where in the primed coordinate system $\alpha$ takes the place of $\theta_2$ and $\phi'$ takes the place of $\phi$. If one holds $\alpha$ fixed while rotating $\vec{b}$ about $\vec{p}$, then $\phi'$ varies from 0° to 360°. We can set the three components of $\vec{b}$ equal to each other:

$$\sin\alpha\cos\phi' = \cos\theta_1\sin\theta_2\cos\phi - \sin\theta_1\cos\theta_2 \tag{5}$$

$$\sin\alpha\sin\phi' = \sin\theta_2\sin\phi \tag{6}$$

$$\cos\alpha = \sin\theta_1\sin\theta_2\cos\phi + \cos\theta_1\cos\theta_2. \tag{7}$$

Using these three equations we can then solve for the projected separation, $\phi$:

$$\tan\phi = \frac{\tan\alpha\sin\phi'}{\sin\theta_1 + \cos\theta_1\tan\alpha\cos\phi'}. \tag{8}$$

Therefore, by assuming an inclination angle $i$, where $\theta_1 = 90 - i$, and assuming a separation angle $\alpha$, we can compute $\phi$ as a function of $\phi'$. As $\phi'$ varies from 0° to 360°, $\phi$ will take on a range of values. The probability density function for $\phi$ can then be derived by making the reasonable assumption that all values of $\phi'$ are equally likely.

We computed the probability density functions (PDFs) for three values of $\alpha$ and 901 equally spaced values of $i$ (0°–90° in steps of 0.1°). In Figure 7 we show these results as three plots, one for each value of $\alpha$. The PDFs are shown in grayscale where dark means most likely value of $\phi$ for each $i$. The black curve shows $\bar{\phi}(i,\alpha)$, the mean value of $\phi$ for each $i$ and $\alpha$ (averaged over all $\phi'$) and the lower (upper) gray curve marks the value of $\phi$ lying above 10% (90%) of the integrated probability for each $i$. The data for our seven cores, taken from Table 4, are superposed on the probability density maps. Recall that for each core the outflow inclination has been used as a proxy for the unknown pseudodisk inclination $i$ (see § 4.1).

From an examination of Figure 7 it is clear that some values of $\alpha$ fit the data better than do others. For $\alpha = 20°$ some points appear in a region forbidden by the models and are far away from the average curve. The opposite extreme happens for $\alpha = 50°$, where two of the points lie below the 10% curve. Qualitatively, $\alpha = 35°$ appears more likely since all points lie near the average curve. Two points lie in the forbidden region, but they are very close to the border, where the PDF is largest.

A rigorous analysis aimed at finding the best-fit $\alpha$ by taking into account the full density distribution as well as the uncertainties in both projected separation $\phi$ and inclination $i$ is beyond the scope of this paper. Instead, we will crudely estimate the best-fit $\alpha$ by minimizing the chi-squared difference between our data and $\bar{\phi}(i,\alpha)$. We created a grid of models with $\alpha$ ranging from 0° to 90° in steps of 0.1°. For each model we computed $\chi^2$, defined as

$$\chi^2 = \sum_{j=1}^{7} \frac{[\phi_j - \bar{\phi}(i,\alpha)]^2}{\sigma^2_{\phi_j}}, \tag{9}$$

where $\phi_j$ is the projected separation for an individual

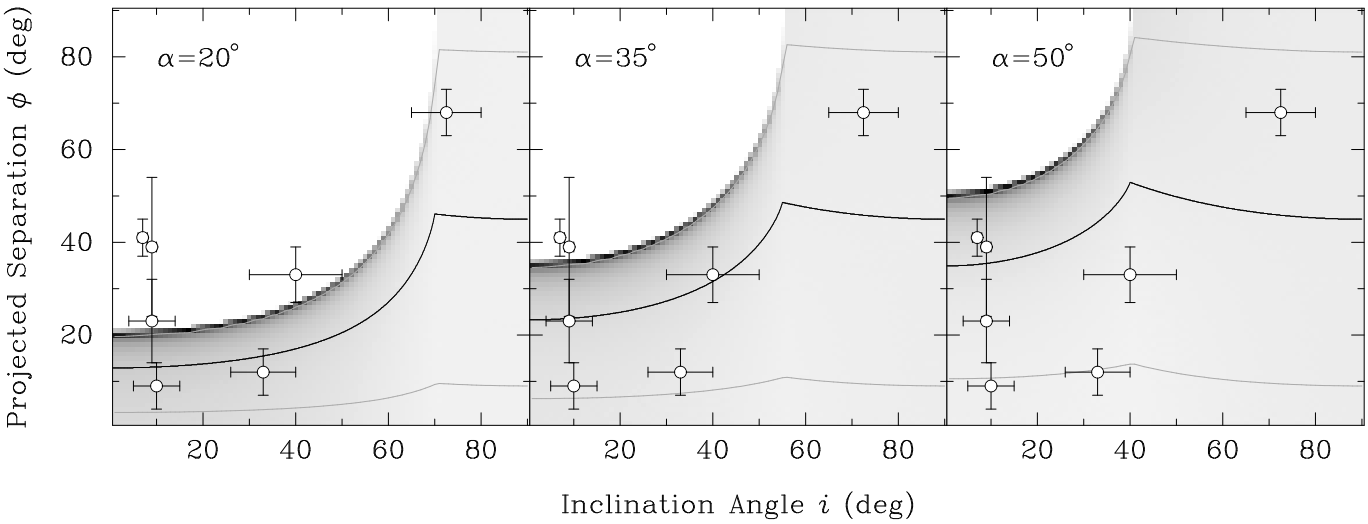


**Figure 7.** Probability density functions (grayscale) of the projected separation angle, $\phi$, between the mean magnetic field and observed pseudodisk symmetry axis as a function of pseudodisk inclination angle $i$. Three intrinsic separation angles, $\alpha$, are shown. ($\alpha$ is defined as the 3D separation angle between the magnetic field and pseudodisk axis.) The black line shows the mean separation angle as a function of inclination. The two gray lines correspond to 10% (lower) and 90% (upper) probability (i.e., for a given inclination the specified percentage of projected separations lie below the given curve). The data points represent the seven cores that have been observed by SHARP. See § 4.2 for details.

source and $\sigma_{\phi_j}$ is the uncertainty in the projected separation. For this simple analysis we set all the $\sigma_{\phi_j}$ to unity when computing $\chi^2$, thereby giving each point equal weight. Thus, our simple approach amounts to a least squares fit to the average curve $\bar{\phi}(i, \alpha)$. The model with the smallest $\chi^2$ has $\alpha = 35.0°$, which is our initial crude estimate for the best-fit value of $\alpha$.

Our analysis method may lead to a bias in our best-fit value for $\alpha$. To see this, note that it favors models in which the data points lie close to the average curve, whereas in reality we expect the data points for a given $i$ to follow a distribution given by the PDF. Our crude approach could thus penalize high values for $\alpha$, for which the data are expected to have a relatively larger spread from the model average curve (see Fig. 7). To explore the magnitude of this possible bias, we carried out Monte Carlo simulations as follows: We adopted an assumed value $\alpha_{true}$, then using the measured inclinations $i$ for our seven sources, we computed from Equation 8 seven values of the projected separation $\phi$ by giving each source a random $\phi'$. We then fit these simulated data to find $\alpha_{fit}$. We repeated this 10,000 times each for $\alpha_{true}$ in the range 20° to 50° in steps of 1°. We then computed the mean $\alpha_{fit}$ for each input $\alpha_{true}$ and fit the data to a straight line to obtain the following relation:

$$\alpha_{true} = 0.91\alpha_{fit} + 4.24°. \quad (10)$$

The mean absolute difference between $\alpha_{true}$ computed via Equation 10 and the value input to the Monte Carlo simulations is only 0.26°. Starting with our initial best-fit $\alpha$ of 35.0°, we used Equation 10 to find a bias-corrected best-fit $\alpha$ of 36.1°.

We are now in a position to compute the probability of obtaining a bias-corrected best-fit $\alpha$ at or below 36.1° by pure chance. We consider the case where $\vec{b}$ points in a random direction in 3D space compared to $\vec{p}$ (see Fig. 6). Note that this is not equivalent to choosing uniformly distributed random values for $\alpha$ and $\phi'$ because such a distribution will sample the unit sphere non-uniformly (the differential unit of surface area is $\sin\alpha\, d\alpha\, d\phi'$). We found that when $\alpha$ and $\phi'$ are chosen such that the unit sphere is sampled uniformly, then the resulting distribution of $\phi$ (computed from Eq. 8) is also uniform, regardless of $\theta_1$. Therefore, generating random directions of $\vec{b}$ reduces to merely generating random values of $\phi$ directly.

We ran 10,000 random $\vec{b}$ Monte Carlo simulations. In each simulation, we held the inclination angles of each of our seven cores fixed at the values shown in Table 4 and Figure 7, and for each core we chose a random value of the projected separation $\phi$ (0° to 90°, uniform distribution). Then we computed the best-fit $\alpha$ for each simulation. Only 4.21% of the models yielded a bias-corrected best-fit $\alpha$ at or below 36.1°. Alternatively, 95.79% of models with random projected separation angles led to a best-fit $\alpha$ greater than 36.1°. Therefore, our analysis indicates that we have detected a positive correlation between the core magnetic field direction and the pseudodisk symmetry axis with ∼96% confidence. Additional sources of error are considered in § 4.5 below, leading to some modifications to the above conclusions regarding $\alpha$ and our confidence level.

### 4.3. *Combining Polarization Maps to Increase Signal-to-Noise*

In the previous subsection we utilized the mean magnetic field direction for each of our seven cores, as computed using $2\sigma$ polarization measurements from Table 2 of the present paper and Table 1 of Paper I. However, our Stokes core maps hold more information than what is contained in just the points with $2\sigma$ detections. We can make use of this information by combining the maps for many cores into a single source-averaged magnetic field map. Such a map will naturally have an enhanced signal-to-noise ratio. Our goal is to compare this com-

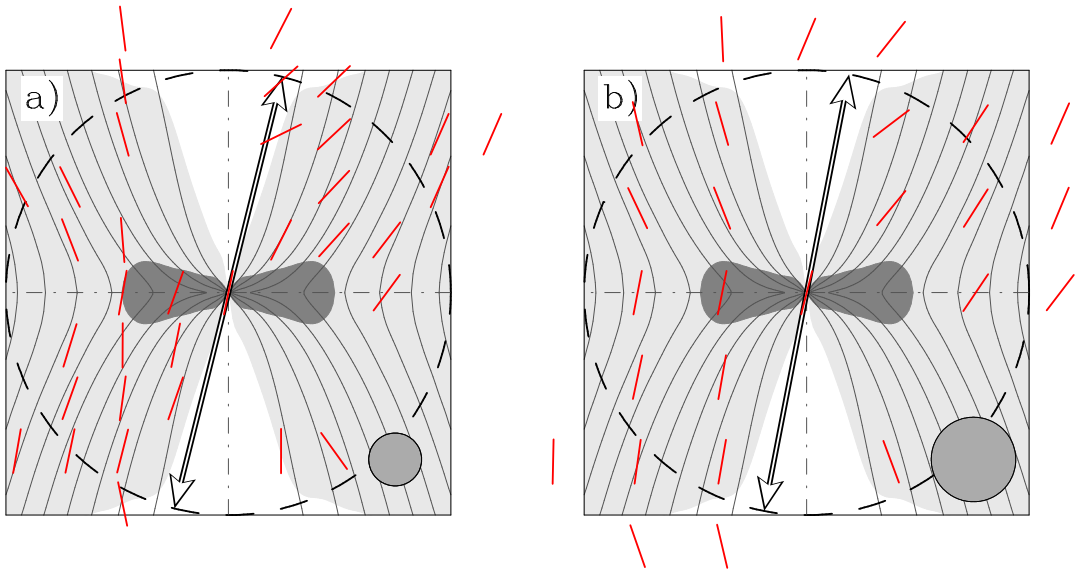


**Figure 8.** Source-averaged magnetic field map (red bars) obtained by combining data from six cores (excluding Serp-FIR1), superposed on Figure 8(c) from Allen et al. (2003a) showing the pseudodisk and magnetic field lines. Before combination, all source maps were rotated so that the pseudodisk axis was horizontal and the blue-shifted lobe of the molecular outflow pointed roughly upward. The gray circle in the bottom right shows the FWHM of the Gaussian kernel used for combining data. *a)* Map obtained using a Gaussian kernel with a FWHM of 0.238 infall radii. The mean magnetic field angle (white outlined vector) is 166° (offset by 14° from the pseudodisk symmetry axis). *b)* Map obtained using a Gaussian kernel with a FWHM of 0.38 infall radii. The mean magnetic field angle is 169° (offset by 11° from the pseudodisk symmetry axis). See § 4.3 for details.

bined map to Figure 8(c) of ALS03, which is the model shown in Figures 1 to 4. As discussed in § 3.5, the high inclination angle of Serp-FIR1 makes this core a poor test of magnetically regulated core-collapse, and also makes it unsuitable for overlaying on Figure 8(c) of ALS03. For these reasons, it is excluded from the following analysis.

We start with the combined maps for Stokes $I$, $Q$, and $U$ and their associated errors for each core (see § 2). We exclude sky positions where the flux is less than 25% of the peak, just as was done in Paper I and in earlier sections of the present paper. Next, we rotate the pixel positions in each core so that the pseudodisk lies horizontal and the blue-shifted lobe of the molecular outflow lies in the top half of the rotated figure. Note that when rotating $Q$ and $U$ by an angle $\theta$, the values become intermixed by a rotation matrix having angle $2\theta$:

$$\begin{bmatrix} Q' \\ U' \end{bmatrix} = \begin{bmatrix} \cos 2\theta & -\sin 2\theta \\ \sin 2\theta & \cos 2\theta \end{bmatrix} \begin{bmatrix} Q \\ U \end{bmatrix}. \qquad (11)$$

We next compute $q = Q/I$ and $u = U/I$ and their associated errors for each core.

Just as for Figs. 1–4, our magnetic field maps must be scaled to account for distance and infall radius before they can be compared with the ALS03 model. Thus, we convert the rotated pixel offsets for each core onto the same scale by dividing the pixel scale in arcseconds ($9\farcs5$) by the core's infall radius measured in arcseconds. The computed pixel scale for each core is given in Table 4. With the combined data from all six cores we have many independent polarization measurements all ready for superposition onto the ALS03 model. Next these measurements need to be combined and sampled on a uniform grid to increase the signal-to-noise.

To combine all these polarization measurements into one polarization map we overlay a grid on the data and at each grid point compute the weighted averages $\bar{q}$ and $\bar{u}$ as well as the associated errors $\sigma_{\bar{q}}$ and $\sigma_{\bar{u}}$. We use a Gaussian kernel with weighting based on distance from the grid point and the errors in the individual measurements. The kernel FWHM is set equal to the grid spacing and we use a cutoff radius also equal to the grid spacing. We have freedom in choosing the grid spacing, so we opt to use both extremes from Table 4, yielding two different source-averaged maps. L483 has the smallest grid spacing (highest resolution) while IC348-SMM2 has the largest spacing (lowest resolution). B335, L1448-IRS2, and L1527 have spacings similar to that of L483 while L1157's spacing is close to that of IC348-SMM2.

After creating regularly sampled maps of $\bar{q}$, $\bar{u}$, $\sigma_{\bar{q}}$, and $\sigma_{\bar{u}}$ we compute the polarization and magnetic field direction using the same techniques, cutoffs, and debiasing as for the analysis described in § 2. We obtain 35 vectors for the high resolution map and 26 for the low resolution map. These magnetic field maps are shown in Figure 8. The gray circles at the bottom right of each panel show the Gaussian kernel used to create each map. We also compute and plot the mean magnetic field direction (Equal Weight Stokes Mean; see § 3.1). The mean field angle is 166° for the data in Figure 8a and 169° for Figure 8b.

The combining of our sources to produce a source-averaged magnetic field map for a Class 0 protostar gives us a better sampling of the characteristic magnetic field structure than was possible for any individual source. The appearance of Figure 8 is consistent with our result from the previous subsection; the mean magnetic field direction is nearly parallel to the pseudodisk symmetry axis (within 15° for both the low- and high-resolution maps). Furthermore, we see hints of a pinch in the field, as predicted by magnetically regulated core-collapse models. The pinch appears to be stronger than predicted on the

right side of each map and weaker than predicted on the left side. Nevertheless, all four quadrants of each map show a tendency for the field to be drawn inward as we approach the pseudodisk plane, in qualitative agreement with model predictions.

### 4.4. *Correlation Between Mean Magnetic Field and Outflow Axis*

Because the outflow axis is strongly correlated with the pseudodisk symmetry axis (§ 4.1) and the pseudodisk symmetry axis is preferentially aligned with the magnetic field (§ 4.2), we anticipate a positive correlation between outflow axis and magnetic field. We can address this quantitatively by repeating the analyses of § 4.2 and § 4.3 using the outflow axis instead of the pseudodisk symmetry axis. When computing the projected separation $\phi$ using the outflow axis, we find the bias-corrected best-fit value of $\alpha_o$ to be 34.4° (here denoted $\alpha_o$ to distinguish it from $\alpha$ computed using the pseudodisk). From Monte Carlo simulations we estimate the probability of obtaining such a value by chance to be 2.87%, corresponding to a confidence level of ∼97%. These results are nearly the same as the values obtained using the pseudodisk axis, which were $\alpha = 36.1°$ and ∼96% confidence. We also stacked and combined the cores, as in § 4.3, but this time rotated each core so that the outflow axis points straight up and down with the blue lobe of the molecular outflow still in the top half of the rotated figure. The mean magnetic field angle is 160° at high resolution and 165° at low resolution. These angles are similar to the 166° and 169° values obtained when setting the observed pseudodisk major axis to be exactly horizontal. Furthermore, the magnetic field maps are nearly identical to those shown in Figure 8. We conclude that we have found evidence of a correlation between magnetic field direction and outflow axis, with a similar degree of confidence as for the pseudodisk-magnetic field correlation discussed earlier.

### 4.5. *Sources of Error*

One possible source of error is the slight difference in selection of vectors between Paper I and the present paper. Paper I considered vectors having $p/\sigma_p \geq 2$ before debiasing to be polarization detections while in the present paper we require vectors to pass that threshold after debiasing. Since debiasing lowers $p/\sigma_p$, when we computed the mean magnetic field angles for Paper I cores we used some vectors that would not have been selected under our new criterion. If we require $p/\sigma_p \geq 2$ after debiasing for the cores in Paper I, we lose five vectors (1 in L1527, 3 in IC348-SMM2, and 1 in B335). Without these vectors, the mean magnetic field angle changes from 49° to 47° in L1527 and from 137° to 147° in IC348-SMM2. There is only one high-flux vector in B335, so applying the stricter criterion results in the loss of this source for analysis, leaving only six sources for fitting $\alpha$. The bias-corrected best-fit $\alpha$ decreases to 31.5° (∼97% confidence) and the bias-corrected best-fit $\alpha_o$ decreases to 26.2° (∼98% confidence). Thus, if we apply the stricter selection criterion to the data from Paper I, the statistical significance of the correlation between mean magnetic field direction and pseudodisk symmetry axis increases slightly. The same is true for the correlation between mean field direction and outflow axis.

In § 2 we discussed the improved error analysis used in the present paper. Is it possible that this improved error analysis, if applied to the data in Paper I, would significantly alter those results? To test this, we reprocessed the data for L1527 using the new method. There are seven polarization detections in common between the old and new methods. The median difference in angle for these seven polarization vector pairs is 5°, which is less than the median uncertainty of 10°. Furthermore, the difference in mean magnetic field angle is less than one degree. Therefore, it does not appear that the change in error analysis method between Paper I and the present paper significantly impacts our results.

Observational uncertainties in inclination angle and projected separation are another source of error. Small variations in these quantities may lead to large changes to our best-fit $\alpha$. To test the robustness of our fits, we again ran Monte Carlo simulations. In each simulation, each source's inclination and projected separation angle were varied randomly using a Gaussian weighting with standard deviation equal to the corresponding errors listed in Table 4. The resulting mean and standard deviation of the bias-corrected best-fit values of $\alpha$ and $\alpha_o$ are $35.4° \pm 3.9°$ and $34.6° \pm 4.5°$, respectively. Therefore, our best-fit $\alpha$ and $\alpha_o$ are robust to within ∼4°. Uncertainties in inclination angle may also impact our estimated confidences. We re-ran the Monte Carlo simulations described in the last two paragraphs of § 4.2, this time allowing the inclination angles to vary with a random Gaussian weighting. The probability of obtaining a bias-corrected best-fit $\alpha$ of less than or equal to 36.1° by pure chance increases to 5.25%, and the probability for $\alpha_o$ increases to 3.92%. Therefore, we downgrade our earlier confidence levels for the pseudodisk-magnetic field and outflow-magnetic field correlations to 95% and 96%, respectively.

Poor sampling of a pinched magnetic field can lead to error in computing the mean field. For example, if in Figure 8 the magnetic field were to be only measured in the upper left and bottom right quadrants, then the computed mean field direction would be biased counterclockwise. Such an error may have occurred for L1527 and B335 (shown in Figures 5 and 7 of Paper I, respectively). If the field in these cores is accurately described by the ALS03 model aligned with the pseudodisk symmetry axis, then the computed mean magnetic field direction in both cores is rotated away from the symmetry axis of the magnetic field by a large angle. This would lead to too-large projected separation values, $\phi$, for these cores. Fitting artificially high values of $\phi$ at low inclination would lead to an overestimate of $\alpha$. Because of this possible source of error, our best-fit values for $\alpha$ and $\alpha_o$ should be treated as rough upper limits rather than best estimates. Folding in the uncertainties discussed in the previous paragraph, we estimate an upper limit on $\alpha$ of $35.4° + 3.9°$ or ∼39°. Similarly, our estimated upper limit on $\alpha_o$ becomes $34.6° + 4.5°$ or ∼39°.

## 5. DISCUSSION

As discussed in § 1, the first prediction of magnetically regulated core-collapse models is that a pseudodisk exists and has its symmetry axis aligned with the core magnetic field. In § 4.2 and § 4.5 we showed that for the cores in our sample the pseudodisk symmetry axis does tend to align

with the mean magnetic field direction ($\alpha < 39°$), and we showed that this result is unlikely to be due to chance. If the pseudodisk symmetry axes and core magnetic fields are indeed preferentially parallel, then we can conclude that interstellar magnetic fields must play a significant role in the collapse of molecular cloud cores. Turbulence may have some effect on this process, but it cannot be strong enough to completely overcome the tendency for organized inward motion of gas along ordered field lines. An important avenue for future research would be to better constrain the pseudodisk-magnetic field misalignment angle $\alpha$, as this angle could serve as a point of comparison between observations and theories.

The second prediction of magnetically regulated core-collapse models is that the magnetic field should be pinched. Our source-averaged map (Figure 8) shows hints of a pinch in agreement with this prediction. Furthermore, it appears that the pinch continues outside of the infall region, although more vectors beyond the infall radius are needed to confirm this result. Observations of the field outside the infall region provide a way to discriminate among magnetically regulated star formation models. For example, the ALS03 model has a gentle pinch outside the infall region while in some other models the field is uniform there (e.g., Galli & Shu 1993a,b). Previous investigations (Li et al. 2009; Ward-Thompson et al. 2009) have found some degree of alignment between the magnetic fields of cloud cores (traced by submillimeter polarization) and the magnetic fields in the surrounding regions of the cloud (traced by optical polarization). An interesting avenue for future research would be to map the magnetic fields in the cloud regions surrounding each of our seven cores, for comparison with the internal core fields mapped by SHARP. Near-infrared polarimeters such as Mimir (Clemens et al. 2007) and SIRPOL (Kandori et al. 2006) can observe polarization of background stars viewed through cloud regions surrounding a core. Furthermore, because they operate at near-IR wavelengths (where the extinction is lower than at optical wavelengths), they can probe denser regions nearer to the cores which generally cannot be studied via optical polarimetry.

In § 4.4 we found that the axes of bipolar outflows are preferentially aligned parallel to core-scale magnetic fields with a rough upper limit on the characteristic misalignment angle, $\alpha_o$, of $\sim$39°. Since the outflow is believed to run parallel to the axis of the Keplerian circumstellar disk (§ 1), our results suggest a preferential alignment between the circumstellar disk rotation axis and the core magnetic field. As discussed in § 1, Joos et al. (2012) have argued that circumstellar disks cannot form unless their axes are misaligned with the core magnetic fields, so it is interesting that our results suggest an upper limit of $\sim$39° on this misalignment. However, it is important to remember that the outflow, pseudodisk, and magnetic field observations discussed in this paper pertain to structures having size scales well above the very small scales ($\sim$few AU) where outflows are believed to be launched. Observations at much higher resolution would seem to be required before we can confidently constrain the alignment of the young circumstellar disks that are presumed to be growing inside Class 0 cores.

Hull et al. (2013) measured 1.3 mm polarization on $\sim$1000 AU scales for a sample of 17 low-mass protostellar cores. (We referred to this work in § 3 above.) Four of these cores are also included in our own survey: L1157, L1448-IRS2, L1527, and Serp-FIR1 (identified as Ser-emb 6 by Hull et al. 2013). Hull et al. (2013) find mean magnetic field position angles of $139 \pm 9°$ in L1157 and $146 \pm 4°$ in L1448-IRS2. These values are consistent with our respective SHARP (larger-scale) magnetic field measurements, within the errorbars (see Table 4). For L1527, their mean magnetic field is $174 \pm 8°$, suggesting a magnetic field which is toroidal, in contrast to the poloidal field geometry claimed in Paper I. This may indicate that the field in L1527 has been wrapped up azimuthally on small scales by core rotation, a possibility discussed by Hull et al. (2013). In the last source, Serp-FIR1, Hull et al. (2013) measure a mean magnetic field position angle of $157 \pm 3°$, nearly perpendicular to our measured value. Since the field measured by Hull et al. (2013) is nearly parallel to the outflow axis (and thus parallel to the presumed rotation axis), azimuthal fields cannot be invoked to explain the difference between their result and ours. As discussed in § 3.5, however, the high inclination angle of Serp-FIR1 makes it a poor test of magnetically regulated core-collapse models. Therefore, results for the four sources in common between Hull et al. (2013) and the present paper are consistent with a picture of magnetic regulation from the large (core) to the small ($\sim$1000 AU) scales, provided that we allow for a transition to toroidal fields on small scales in L1527.

For their full sample of 17 cores, Hull et al. (2013) found no correlation between the mean magnetic field directions and the protostellar outflow axes. Assuming that the outflows run parallel to the axes of the circumstellar disks, then the Hull et al. (2013) results imply that the disk rotation axes are not aligned with the $\sim$1000 AU scale magnetic fields. Their results differ from our own, since we do find a correlation between magnetic field direction and outflow axis. We consider three possibilities to resolve this apparent discrepancy. First, if some of the 17 cores have toroidal small-scale fields while others are poloidal, then this would lead to a poor correlation between outflow axis and field direction. Hull et al. (2013) consider this explanation to be insufficient, since it would lead to a bimodal distribution for the projected angle between outflow and magnetic field, whereas the observed distribution is mostly consistent with a random distribution rather than a bimodal one. A second possibility, also discussed by Hull et al. (2013), is that their sample includes multiples which present a more complex situation than what has been modeled (e.g., by ALS03), and thus may obscure any correlation between outflow axis and field direction. Lastly, it is important to remember that the $\sim$1000 AU size scales mapped by Hull et al. (2013) are considerably smaller than the $\sim$10,000 AU scales mapped in the present paper. It is possible that the magnetic field may be ordered on large scales but scrambled on smaller scales, due to some combination of rotational, pinching, and outflow motions. More work is needed to understand the apparent discrepancy between the results of Hull et al. (2013) and our own.

## 6. SUMMARY

We presented 350 $\mu$m polarization maps of four low-mass cores with Class 0 protostars: L483, L1157, L1448-

IRS2, and Serp-FIR1. We created a larger sample by combining these results with Paper I results for three similar cores: B335, L1527, and IC348-SMM2. With this sample we were able to test magnetically regulated models of core-collapse using sources most directly comparable with the models; i.e. isolated, single, young low-mass cores with outflow axes lying close to the plane of the sky. This last point is very important because projection effects can come into play when comparing sky plane components of 3D axes. Six of the sources have their outflow axes oriented closer to the plane of the sky than to the line of sight, while one, Serp-FIR1, has its outflow almost along the line of sight. The results from our sample of seven cores are as follows:

1. In § 4.1 we showed that for the six sources with identified pseudodisks, the mean difference in position angle between the outflow axis and the pseudodisk symmetry axis (i.e., pseudodisk apparent minor axis) is 12°. This gives us confidence in using the outflow inclination angle as a proxy for the pseudodisk inclination angle. Furthermore, for Serp-FIR1, which has no apparent pseudodisk axis, we used the position angle of the outflow as a proxy for the position angle of the pseudodisk symmetry axis. In § 4.2 we used our polarization data, the observed position angles of the pseudodisk symmetry axes for six of our sources, and the above proxies, to test for a correlation in 3D space between pseudodisk symmetry axis and core magnetic field. Using a simple least-squares analysis, we estimated the 3D separation angle $\alpha$ between these two quantities to be 36°. Our estimate for the probability of obtaining an $\alpha$ less than or equal to 36° by pure chance is about 4%. In § 4.5 we modified these conclusions after addressing additional sources of error. The revised probability for our correlation being due to chance is 5%. Our revised constraint for $\alpha$ is a rough upper limit of 39°.

2. In § 4.3 we combined polarization data for six of the seven sources into a source-averaged magnetic field map. We excluded Serp-FIR1 because its high inclination angle makes it a poor test of the basic predictions of magnetically regulated models. Both the low- and high-resolution versions of our source-averaged map have many more polarization detections than any of the individual maps. The mean magnetic field direction in each of the two source-averaged maps is closely aligned (within 15°) with the pseudodisk symmetry axis. This is consistent with our claimed correlation between the magnetic and pseudodisk symmetry axes. The magnetic field in the source-averaged maps shows hints of a pinch, as predicted by the magnetically regulated models.

3. In § 4.4, using techniques similar to those summarized in point 1 above, we found a correlation between the outflow axis and the core magnetic field direction. As discussed in § 4.5, our crude estimate for the confidence level is ∼96% and our rough upper limit on the misalignment angle $\alpha_o$ is ∼39°.

If our claimed detection of a positive correlation between core magnetic field direction and pseudodisk symmetry axis is correct, then magnetic fields must be strong enough to direct gas infall even in the presence of turbulence. Stronger turbulence should lead to higher values for the misalignment angle $\alpha$, for which we have set the rough upper limit of 39°. Our claimed detection of a positive correlation between core magnetic field direction and bipolar outflow axis might constrain theories for the formation of circumstellar disks, but higher resolution observations are probably required to observationally characterize this.

We thank the anonymous referee for providing useful feedback that improved the statistical analysis in this paper. This material is based upon work at the Caltech Submillimeter Observatory, which is operated by the California Institute of Technology under cooperative agreement with the National Science Foundation (AST-0838261). This research was carried out in part at the Jet Propulsion Laboratory, which is operated by the California Institute of Technology under contract with NASA. We are grateful to the National Science Foundation for supporting the operation of SHARP via grant AST-0909030. N.L.C. is also supported under this grant.

REFERENCES

Allen, A., Li, Z.-Y., & Shu, F. H. 2003a, ApJ, 599, 363
Allen, A., Shu, F. H., & Li, Z.-Y. 2003b, ApJ, 599, 351
Attard, M., Houde, M., Novak, G., et al. 2009, ApJ, 702, 1584
Chen, X., Arce, H. G., Zhang, Q., et al. 2010, ApJ, 715, 1344
Chiang, H.-F., Looney, L. W., Tobin, J. J., & Hartmann, L. 2010, ApJ, 709, 470
Clemens, D. P., Sarcia, D., Grabau, A., et al. 2007, PASP, 119, 1385
Cox, M. G., Eiø, C., Mana, G., & Pennecchi, F. 2006, Metrologia, 43, S268
Davidson, J. A., Novak, G., Matthews, T. G., et al. 2011, ApJ, 732, 97
Davis, C. J., & Eisloeffel, J. 1995, A&A, 300, 851
Davis, C. J., Scholz, P., Lucas, P., Smith, M. D., & Adamson, A. 2008, MNRAS, 387, 954
Dotson, J. L., Vaillancourt, J. E., Kirby, L., et al. 2010, ApJS, 186, 406
Dowell, C. D., Allen, C. A., Babu, R. S., et al. 2003, in Proc. SPIE, Vol. 4855, 73
Dzib, S., Loinard, L., Mioduszewski, A. J., et al. 2010, ApJ, 718, 610
Eiroa, C., Djupvik, A. A., & Casali, M. M. 2008, The Serpens Molecular Cloud, ed. B. Reipurth, 693
Enoch, M. L., Corder, S., Dunham, M. M., & Duchêne, G. 2009, ApJ, 707, 103
Federrath, C., & Klessen, R. S. 2013, ApJ, 763, 51
Fuller, G. A., Lada, E. A., Masson, C. R., & Myers, P. C. 1995, ApJ, 453, 754
Fuller, G. A., & Wootten, A. 2000, ApJ, 534, 854
Galli, D., & Shu, F. H. 1993a, ApJ, 417, 220
—. 1993b, ApJ, 417, 243
Girart, J. M., Rao, R., & Marrone, D. P. 2006, Science, 313, 812
Gueth, F., Guilloteau, S., & Bachiller, R. 1996, A&A, 307, 891
Gueth, F., Guilloteau, S., Dutrey, A., & Bachiller, R. 1997, A&A, 323, 943
Harvey, P. M., Rebull, L. M., Brooke, T., et al. 2007, ApJ, 663, 1139
Hatchell, J., Fuller, G. A., & Ladd, E. F. 1999, A&A, 344, 687
Henning, T., Wolf, S., Launhardt, R., & Waters, R. 2001, ApJ, 561, 871
Hildebrand, R. H., Davidson, J. A., Dotson, J. L., et al. 2000, PASP, 112, 1215
Hirota, T., Honma, M., Imai, H., et al. 2011, PASJ, 63, 1
Hogerheijde, M. R., van Dishoeck, E. F., Salverda, J. M., & Blake, G. A. 1999, ApJ, 513, 350
Hull, C. L. H., Plambeck, R. L., Bolatto, A. D., et al. 2013, ApJ, 768, 159
Hurt, R. L., & Barsony, M. 1996, ApJ, 460, L45
Joos, M., Hennebelle, P., & Ciardi, A. 2012, A&A, 543, A128
Jørgensen, J. K. 2004, A&A, 424, 589

Kandori, R., Kusakabe, N., Tamura, M., et al. 2006, in Proc. SPIE, Vol. 6269, 626951
Kirk, J. M., Ward-Thompson, D., Di Francesco, J., et al. 2009, ApJS, 185, 198
Konigl, A., & Pudritz, R. E. 2000, Protostars and Planets IV, 759
Kun, M. 1998, ApJS, 115, 59
Kwon, W., Looney, L. W., Mundy, L. G., Chiang, H.-F., & Kemball, A. J. 2009, ApJ, 696, 841
Lazarian, A. 2007, J. Quant. Spec. Radiat. Transf., 106, 225
Li, H., Dowell, C. D., Kirby, L., Novak, G., & Vaillancourt, J. E. 2008, Appl. Opt., 47, 422
Li, H., Griffin, G. S., Krejny, M., et al. 2006, ApJ, 648, 340
Li, H.-b., Dowell, C. D., Goodman, A., Hildebrand, R., & Novak, G. 2009, ApJ, 704, 891
Looney, L. W., Tobin, J. J., & Kwon, W. 2007, ApJ, 670, L131
Matthews, B. C., McPhee, C. A., Fissel, L. M., & Curran, R. L. 2009, ApJS, 182, 143
McKee, C. F., & Ostriker, E. C. 2007, ARA&A, 45, 565
Mellon, R. R., & Li, Z.-Y. 2008, ApJ, 681, 1356
Ménard, F., & Duchêne, G. 2004, A&A, 425, 973
Moriarty-Schieven, G. H., & Snell, R. L. 1989, ApJ, 338, 952
Mouschovias, T. C., & Paleologou, E. V. 1979, ApJ, 230, 204
Myers, P. C., Bachiller, R., Caselli, P., et al. 1995, ApJ, 449, L65
O'Linger, J., Wolf-Chase, G., Barsony, M., & Ward-Thompson, D. 1999, ApJ, 515, 696
Park, Y.-S., Panis, J.-F., Ohashi, N., Choi, M., & Minh, Y. C. 2000, ApJ, 542, 344
Prato, L., Rice, E. L., & Dame, T. M. 2008, Where are all the Young Stars in Aquila?, ed. B. Reipurth, 18
Rodriguez, L. F., Curiel, S., Moran, J. M., et al. 1989, ApJ, 346, L85
Shu, F. H., Adams, F. C., & Lizano, S. 1987, ARA&A, 25, 23
Shu, F. H., Li, Z.-Y., & Allen, A. 2004, ApJ, 601, 930
Shu, F. H., Najita, J. R., Shang, H., & Li, Z.-Y. 2000, Protostars and Planets IV, 789
Straizys, V., Cernis, K., Kazlauskas, A., & Meistas, E. 1992, Baltic Astronomy, 1, 149
Tafalla, M., Myers, P. C., Mardones, D., & Bachiller, R. 2000, A&A, 359, 967
Targon, C. G., Rodrigues, C. V., Cerqueira, A. H., & Hickel, G. R. 2011, ApJ, 743, 54
Tobin, J. J., Hartmann, L., Looney, L. W., & Chiang, H.-F. 2010, ApJ, 712, 1010
Tobin, J. J., Looney, L. W., Mundy, L. G., Kwon, W., & Hamidouche, M. 2007, ApJ, 659, 1404
Tomisaka, K. 1998, ApJ, 502, L163
Vaillancourt, J. E. 2006, PASP, 118, 1340
Vallée, J. P., Greaves, J. S., & Fiege, J. D. 2003, ApJ, 588, 910
Viotti, R. 1969, Mem. Soc. Astron. Italiana, 40, 75
Ward-Thompson, D., Sen, A. K., Kirk, J. M., & Nutter, D. 2009, MNRAS, 398, 394
Whitney, B. A., Wood, K., Bjorkman, J. E., & Cohen, M. 2003a, ApJ, 598, 1079
Whitney, B. A., Wood, K., Bjorkman, J. E., & Wolff, M. J. 2003b, ApJ, 591, 1049
Williams, J. P., & Myers, P. C. 2000, ApJ, 537, 891
Wolf, S., Launhardt, R., & Henning, T. 2003, ApJ, 592, 233
Zhou, S., Evans, II, N. J., & Wang, Y. 1996, ApJ, 466, 296